Structural and electrical properties of titanium-doped yttrium niobate

P. Winiarz[1]*, A. Mielewczyk-Gryń[1], S. Wachowski[1], P. Jasiński[2], A. Witkowska[1], M. Gazda[1]

[1]Faculty of Applied Physics and Mathematics, Gdańsk University of Technology, Narutowicza 11/12, 80-233 Gdańsk, Poland

[2]Faculty of Electronics, Telecommunications and Informatics, Gdańsk University of Technology, Narutowicza 11/12, 80-233 Gdańsk, Poland

*corresponding author: piotr.winiarz@pg.gda.pl, Address: Narutowicza 11/12, 80-233 Gdańsk, Poland

Postprint of: Winiarz P., Mielewczyk-Gryń A., Wachowski S., Jasiński P., Witkowska A., Gazda M.: Structural and electrical properties of titanium-doped yttrium niobate. JOURNAL OF ALLOYS AND COMPOUNDS. Vol. 767, (2018), p. 1186-1195. DOI: 10.1016/j.jallcom.2018.07.134

Abstract

In this work, the influence of the substitution of niobium by titanium in $Y_3Nb_{1-x}Ti_xO_{7-\delta}$ on the structural and electrical properties is reported. Several experimental techniques, i.e. X-Ray Diffraction (XRD), Scanning Electron Microscopy (SEM), X-Ray Photoelectron Spectroscopy (XPS) and Electrochemical Impedance Spectroscopy (EIS), were applied to investigate the system $Y_3Nb_{1-x}Ti_xO_{7-\delta}$. Titanium in $Y_3Nb_{1-x}Ti_xO_{7-\delta}$ is an acceptor-type dopant which charge is mainly compensated by oxygen vacancies, moreover, it may adopt different valence states, therefore, oxygen ion-, proton- and electronic-type conductivity are expected. Very interesting, non-monotonic changes in electrical and structural properties as a function of titanium content were observed. The competition between the increasing charge carrier concentration and structural phenomena such as short-range pyrochlore ordering and/or vacancy clustering was proposed as responsible for this non-monotonicity.

Keywords: yttrium niobate, defect fluorite structure, ionic conductivity, protonic conductivity

1. Introduction

Rare earth niobates with a fluorite structure are functional ceramics, which have been recently investigated as materials with considerably high ionic conductivity [1,2]. For instance, oxygen ion conductivities of Y_3NbO_7, $Zr_{1.92}Y_{0.08}O_{2-\delta}$ and $Ce_{0.8}Sm_{0.2}O_{2-\delta}$ are 3.5 x 10^{-5} S cm^{-1} at 800°C [3], 3.7 x 10^{-3} S cm^{-1} at 700°C [4] and 7.2 x 10^{-2} S cm^{-1} at 550°C [5], respectively.

Moreover, the rare earth niobates for the last decade have attracted lots of attention because of their structural features. The structure being significantly dependent on the ionic radius of rare earth cation vary from pyrochlore for bigger cations to intrinsically disordered fluorite for smaller ones [6]. Lopez-Conesa et al. in TEM/SAED studies have shown interesting ordering phenomena within the whole range of rare earth niobates – the existence of short-range pyrochlore ordering for smaller rare earth cations accompanying the long-range fluorite ordering [7]. Furthermore, it has been reported that these compounds are stable in a broad range of oxygen partial pressures [8]. Some fluorite-related compounds, e.g. Ce_3MO_7 (M=Nb or Ta), exhibit a cation ordering which occurs in the metal sublattice. The MO_6 octahedra, in which M^{5+} cations are coordinated with six O^{2-} anions, form the chains along c-axis [9].

Y_3NbO_7 crystallizes in a defect-fluorite type structure ($Fm\bar{3}m$) with a = 5.25Å [10]. This structure derived from the ideal AB_2 fluorite structure, is formed when four tetravalent ions are substituted by three trivalent ions and one pentavalent ion. The charge neutrality requires that one oxygen site in the unit cell is not occupied. This intrinsic oxygen vacancy concentration renders these oxides interesting as oxygen ion conductors. Furthermore, Chesnaud et al. [8] have shown that in Y_3NbO_7 a small concentration of protons are incorporated into the structure when water vapour is introduced and the material exhibits proton conductivity.

Only a few reports in the literature have been devoted to the studies of the factors influencing ionic conductivity of the Y_3NbO_7 system [3,8,11,12]. Yamamura et al. [3] have shown that incorporation of acceptor substitutions, both in the rare earth and niobium sublattices, leads to an increase of oxygen vacancy concentration and ionic conductivity with simultaneous decrease of activation energy. The authors suggested that the unit cell free volume plays an important role in the oxygen ion conduction. Kobayashi et al. [11] have found that the conductivity of the Y_3NbO_7 ceramics increased almost linearly with an increase of the oxygen vacancies concentration. Recently, Marrocchelli et al. [13] carried out molecular dynamics (MD) simulation of the $Zr_{0.5-0.5x}Y_{0.5+0.25x}Nb_{0.25x}O_{1.75}$ oxide, which crystallizes in the defect-fluorite structure. They have found that the interplay between several factors like ionic radii, defect charge, lattice strain, local cation ordering, vacancy-vacancy interaction and vacancy-cation interaction influences the ionic conductivity. The MD results, as well as the results of reversed Monte Carlo (RMC) analysis of neutron diffraction data, showed that the Nb-O bonds are significantly shorter (1.96 Å) than the Y-O ones (2.28 Å) [14]. This is caused by the higher charge of the Nb^{5+} cation in comparison to the Y^{3+} ion. The oxides of a defect-fluorite structure in which the cation charge difference is lower (e.g. $Zr_2Y_2O_7$) show higher ion conductivity than Y_3NbO_7. Therefore, it may be expected that partial substitution of niobium with a cation of the valence lower than +5, could lead to an increase of ionic conductivity of Y_3NbO_7. It should be noted that apart from decreasing the local strain such a substitution should also increase the concentration of oxygen vacancies.

In this work, the influence of the substitution of niobium by titanium in $Y_3Nb_{1-x}Ti_xO_{7-\delta}$ on the structural and electrical properties is reported for the first time. A special attention has been devoted to the structural properties and ionic conductivity. Both oxygen ions and protons have been considered as potential charge carriers. Moreover, since titanium may adopt different valence states, a possibility of using titanium substituted yttrium niobate as a triple conducting oxide was discussed.

2. Experimental

The $Y_3Nb_{1-x}Ti_xO_{7-\delta}$ (x = 0 to 0.20) were synthesized through a solid-state synthesis route. Stoichiometric amounts of powders (Y_2O_3 Alfa Aesar 99.99%; Nb_2O_5 Alfa Aesar 99.9985%; TiO_2 Prolabo min. 99%) were mixed together in an agate mortar. The resulting powder was uniaxially pressed in a 12 mm mould using the pressure of 520 MPa to obtain pellets. The pellets were heat-treated in three steps. First, they were heated at 1350°C for 8 h, in the second step the heat treatment was performed at 1400°C for 12 h and the final sintering was at 1500°C for 14 h. Between each of the heat treatments, the pellets were ground in an agate mortar and re-pelletized. The heating rate of each stage was 3°C/min.

Structural characterization was performed by X-ray diffraction (XRD) using X'Pert Phillips diffractometer with Cu Kα radiation λ=1.541 Å. The patterns obtained for the single-phase materials were analysed with Rietveld method. As an initial point of the analysis, unit cell parameters of the fluorite structure (space group no. 225) [15] were used. Pseudo – Voigt peak shape function was used to model the profile.

In order to determine the valency states of the elements, XPS measurements were carried out for Y_3NbO_7 and $Y_3Nb_{0.85}Ti_{0.15}O_{7-\delta}$. X-Ray photoelectron spectra were carried out on Omicron spectrometer. Non-monochromatic source of Mg Kα (1253.6 eV) was used. The samples for the structural and XPS analysis were pulverized prior to the measurements and put on a carbon tape. The pressure in the chamber was 10^{-10} mbar, anode voltage was 15 kV and the emission current 20 mA giving the power of radiation equal to 300 W. The fitting of XPS curves was performed using XPSPeak4.1 software [16]. As a reference for charge accumulation compensation, C 1s binding energy was set to 284.5 eV. The Shirley type background was subtracted from the spectra.

The microstructure of sintered pellets was examined on FEI Quanta FEG 250 Scanning Electron Microscope (SEM). Images of surfaces and fractures were taken in high vacuum mode using Everhart-Thornley Detector working in secondary electrons mode. Additionally, samples were checked towards secondary phases formation by imaging of polished samples with Back-Scattered Electrons Detector. The average grain size d_{avg} were measured by the grain intercept method described elsewhere [17]. Fracture images were used to determine grain sizes. Density measurements were performed using Archimedes principle with kerosene (ρ=0.8142 g/cm^3) as a medium.

Electrochemical Impedance Spectroscopy (EIS) measurements were carried out using Solartron SI 1260 frequency analyser. The platinum electrodes were deposited by paint-brushing ESL 5542 paste. Additionally, platinum wires ϕ=0.15mm were attached on both sides of the sample. The samples with the electrodes were then heated at 900°C for 1 h. EIS data were measured in a frequency range from 1Hz to 1MHz and excitation voltage amplitude of 1000 mV. The data were taken in the temperature range of 350–750 °C, with 50 °C step, in the dry and wet air and the dry and wet hydrogen. The results were analysed with ZView software (Scribner Associates, Inc.). Equivalent circuits consisting of a combination of (*RQ*) elements in series were used to model the spectra. The constant phase element *Q* depends on the impedance according to the formula $1/Z = Y = Q_0(j\omega)^n$, where the admittance Q_0 and the angle of misalignment, *n*, are the fitted parameters. From these parameters and the measured resistance, pseudo-capacitances was calculated for each semicircle by using the formula [18]:

$$C = Q_0^{\frac{1}{n}} R^{\frac{1}{n}-1} \tag{1}$$

The *C* value was then used to identify charge transport processes. The semicircle with the lowest pseudo-capacitance is typically attributed to the grain interior (bulk), whereas the next lowest is attributed to grain boundary conductivity. In this way, the grain and grain boundary conductivity values were determined. Electrode responses were present but were considered not relevant to the current investigation.

3. Results

The XRD patterns of $Y_3Nb_{1-x}Ti_xO_{7-\delta}$ powders are presented in Fig. 1. All of the reflections observed for the samples with $x \leq 0.15$ (Fig.1.a) were indexed within the defect-fluorite structure. The enlarged fragments of the patterns of $Y_3Nb_{0.85}Ti_{0.15}O_{7-\delta}$, $Y_3Nb_{0.82}Ti_{0.18}O_{7-\delta}$ and $Y_3Nb_{0.8}Ti_{0.2}O_{7-\delta}$ (Fig.1.b) show that apart from the defect-fluorite phase also a small amount of Y_2TiO_5 is present in the samples with $x > 0.15$. This suggests that the solubility limit of titanium in $Y_3Nb_{1-x}Ti_xO_{7-\delta}$ is exceeded in the sample with 0.18 and 0.20 Ti content. In order to study the materials relatively far from the solubility limit of titanium, we concentrated the studies on the materials with $x \leq 0.15$.

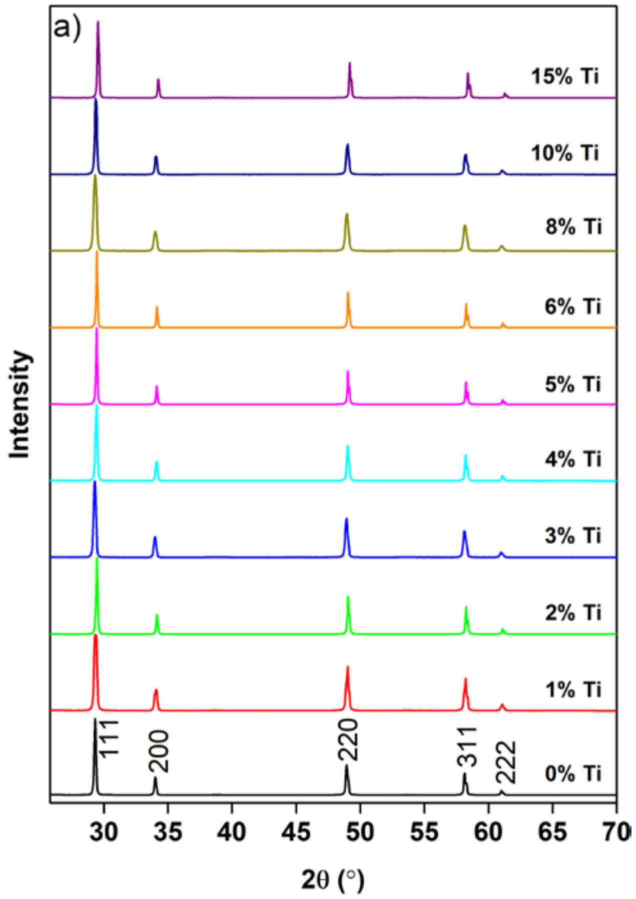

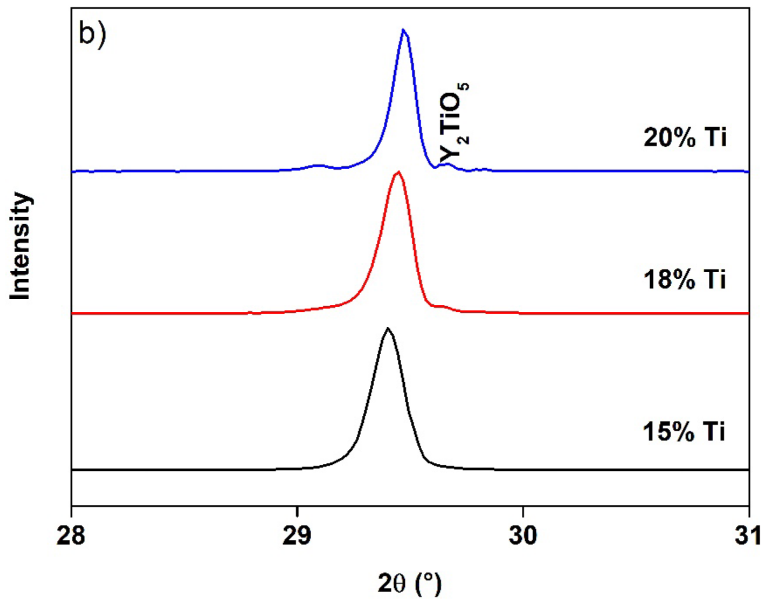

Fig. 1 a) XRD patterns of $Y_3Nb_{1-x}Ti_xO_{7-\delta}$, where x = 0 to x = 0.15,

b) enlargement of the XRD patterns of $Y_3Nb_{1-x}Ti_xO_{7-\delta}$ for x = 0.15, x = 0.18 and x = 0.20.

The XRD results were analysed with the Rietveld refinement method. Examples of the fitted profiles of the a) $Y_3Nb_{0.95}Ti_{0.05}O_{7-\delta}$ and (b) $Y_3Nb_{0.90}Ti_{0.10}O_{7-\delta}$, as well as the difference plots are presented in Fig. 2. The quality of the Rietveld profiles (R_{wp} value) was between 7.3 and 11.7 %. Refined unit cell parameters a, volumes V, agreement indices R_{wp} as well as actual ρ_{rel} and theoretical ρ_t densities and average crystallite sizes d_{avg} of the $Y_3Nb_{1-x}Ti_xO_{7-\delta}$ compounds are collected in Table 1. It can be seen that the unit cell parameter generally decreases with the titanium content, however, the dependence is not strictly monotonic (cf. Fig. 10).

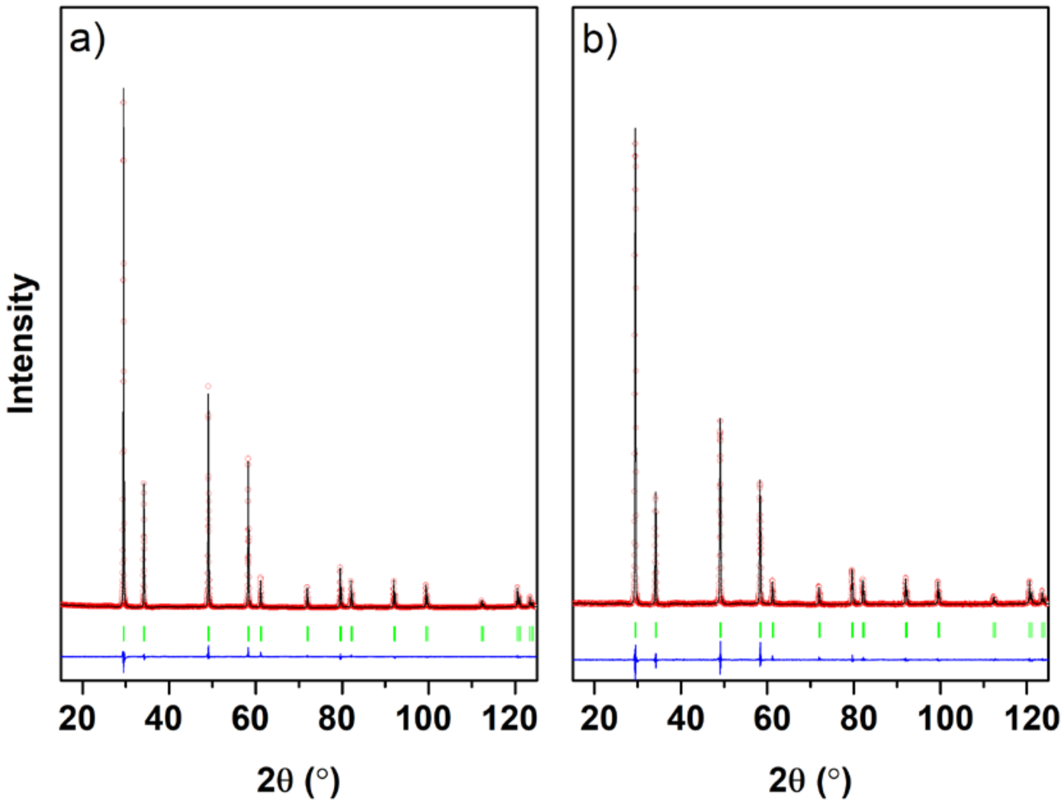

Fig. 2 The Rietveld profiles of the patterns and the difference plots for a) $Y_3Nb_{0.95}Ti_{0.05}O_{7-\delta}$ and b) $Y_3Nb_{0.90}Ti_{0.10}O_{7-\delta}$.

Table 1 Selected structural and microstructural parameters of the $Y_3Nb_{1-x}Ti_xO_{7-\delta}$ samples.

Sample	**a (Å)**	**V (Å^3)**	**R_{wp} (%)**	**ρ_t (g/cm^3)**	**ρ_{rel} (%)**	**d_{avg} (μm)**
Y_3NbO_7	5.2495(1)	144.7(1)	9.9	5.41(1)	82(4)	2.0(3)
$Y_3Nb_{0.99}Ti_{0.01}O_{7-\delta}$	5.2500(1)	144.7(1)	11.4	5.41(1)	72(3)	1.0(1)
$Y_3Nb_{0.98}Ti_{0.02}O_{7-\delta}$	5.2492(1)	144.6(1)	10.5	5.42(1)	72(3)	0.9(2)
$Y_3Nb_{0.97}Ti_{0.03}O_{7-\delta}$	5.2496(1)	144.7(1)	11.7	5.42(1)	73(3)	1.1(1)
$Y_3Nb_{0.96}Ti_{0.04}O_{7-\delta}$	5.2492(1)	144.6(1)	8.6	5.42(1)	72(3)	1.0(1)
$Y_3Nb_{0.95}Ti_{0.05}O_{7-\delta}$	5.2479(1)	144.5(1)	8.2	5.43(1)	82(5)	1.2(1)
$Y_3Nb_{0.94}Ti_{0.06}O_{7-\delta}$	5.2472(1)	144.5(1)	11.1	5.43(1)	72(4)	1.3(2)
$Y_3Nb_{0.92}Ti_{0.08}O_{7-\delta}$	5.2472(1)	144.5(1)	7.3	5.44(1)	73(3)	0.9(2)
$_3Nb_{0.90}Ti_{0.10}O_{7-\delta}$	5.2457(1)	144.4(1)	11.1	5.45(1)	84(9)	1.1(1)
$_3Nb_{0.85}Ti_{0.15}O_{7-\delta}$	5.2421(1)	143.9(1)	11.1	5.47(1)	88(8)	1.1(1)

Scanning Electron Microscope micrographs of the surface and fracture of the studied samples are presented in Fig. 3. The size of crystal grains visible in the micrographs varies between 0.5 μm to

5 µm. The average grain size determined by the intercept method (cf. Table 1) in the samples doped with titanium is close to 1 µm whereas in the Y_3NbO_7 sample it was about 2 µm. Fracture images show that open and closed porosity is present in the volume of the samples. The actual density ρ_{rel} (cf. Table 1) was between 72% and 88%.

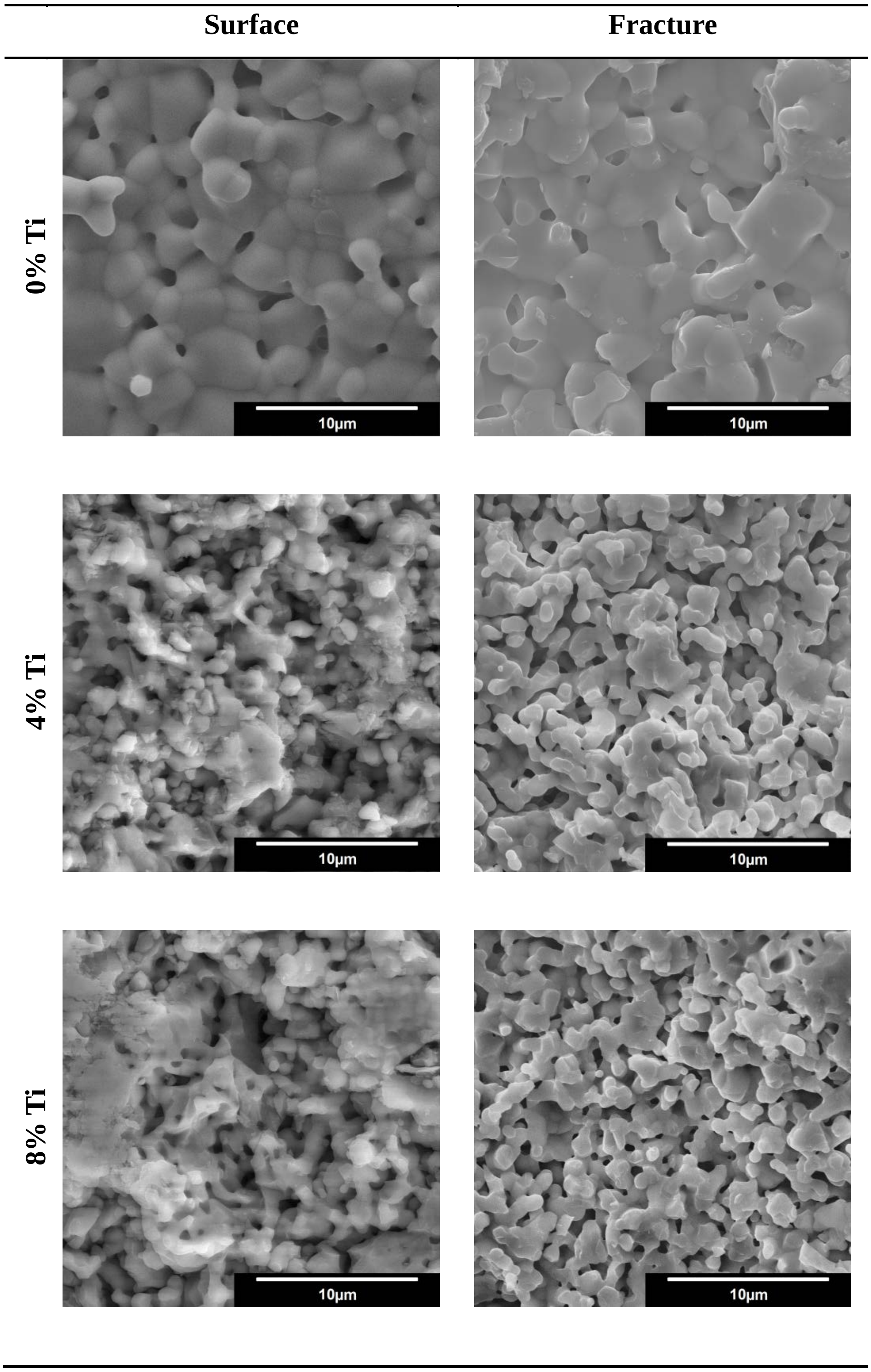

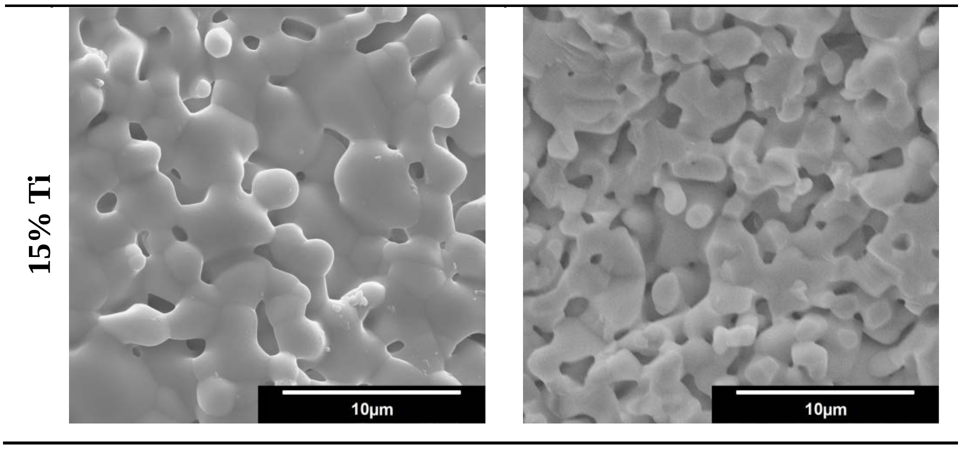

Fig. 3 SEM images of the surfaces and fractures of the samples with different titanium content.

The results of the XPS measurements for $Y_3Nb_{0.85}Ti_{0.15}O_{7-\delta}$ are presented in Figures 4 and 5. The survey spectrum is shown in Fig. 4, whereas Fig. 5 presents peaks corresponding to Y, and Nb. In the survey spectrum, the peaks denoted with a star correspond to a Scotch tape. The positions of the peaks indicate that the valence states of Y and Nb are 3+ and 5+, respectively [19]. The Ti 2p XPS spectrum was very weak. The ratio of Ti3+ to Ti4+ was estimated to $r_{Ti3+/Ti4+}$ = (0.2 ± 0.1). However, the presence of Ti+3 in oxides usually requires annealing in reducing conditions. We believe that if there is any 3+ titanium present it is only a surface effect caused by the surface oxygen depletion in vacuum conditions. Moreover, the preliminary results from X-Ray Absorption Spectroscopy technique (XAS), which have not been published yet, clearly indicate that only Ti4+ is present in the volume of the material. The O1s and Ti2p spectra confirm the valence states of Nb, Y and that the amount of Ti+4 is higher than Ti+3.

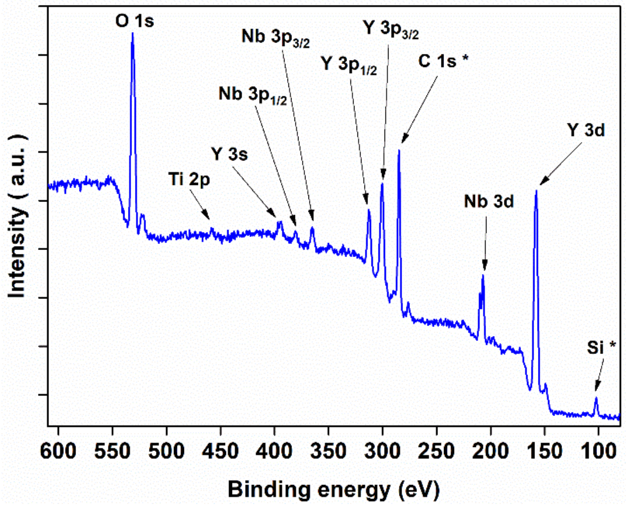

Fig. 4 XPS survey spectrum of $Y_3Nb_{0.85}Ti_{0.15}O_{7-\delta}$.

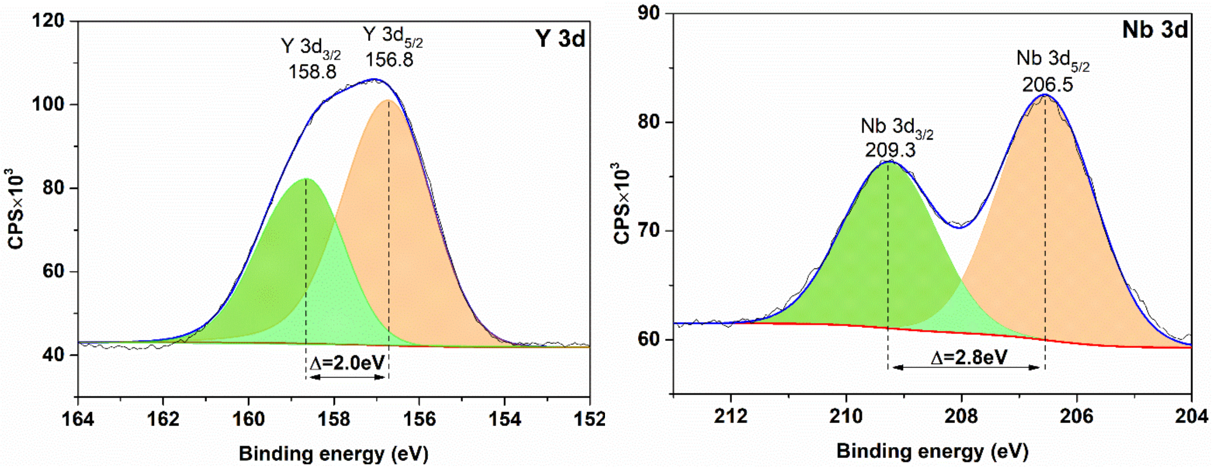

Fig.5 Y 3d, and Nb 3d XPS spectra for $Y_3Nb_{0.85}Ti_{0.15}O_{7-\delta}$. Positions of maxima and doublet split are indicated.

Figure 6 represents an example of the impedance plots obtained for Y_3NbO_7 and $Y_3Nb_{0.85}Ti_{0.15}O_{7-\delta}$ at 750 °C. It can be seen that the $Y_3Nb_{0.85}Ti_{0.15}O_{7-\delta}$ sample exhibits lower impedance in comparison with Y_3NbO_7. In order to properly interpret the data, the model equivalent circuit shown in the figure was applied for the determination of the material conductivity. The circuit consists of two (*RQ*) elements, which represent the observed complex impedance plots quite well. Typical pseudo-capacitance values calculated for the high-frequency semicircle were in the range of 0.6 to 7 × 10^{-11} Fcm^{-1}, whereas in the low-frequency range the values were of the order of 10^{-9} or higher. Therefore, the semicircle at high frequencies was identified as the grain contribution. Moreover, since the pseudo-capacitance values obtained for lower frequency were typical of charge transfer process [20], it is reasonable that the grain boundary contribution is not observed in the measurements. The tails visible in the complex plots are related to the electrode processes. It is in agreement with the report of Yamamura et al. [3].

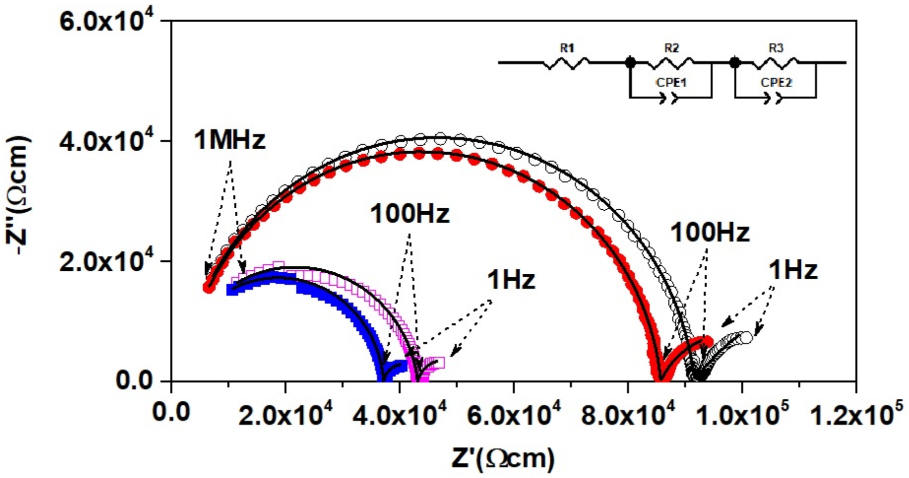

Fig. 6 Complex impedance plots of Y_3NbO_7 (circles) and $Y_3Nb_{0.85}Ti_{0.15}O_{7-\delta}$ (squares) at 750°C in dry (open symbols) and (closed) wet air. The solid lines represent fitted data, and the inset shows the equivalent circuit used for analysis.

The fitted parameters of the data shown in the Fig. 6 are collected in table 2.

Table 2 Fitted parameters for measurements shown in the Fig.6.

Sample	**R1 (Ω)**	**R2 (Ω)**	**R3 (Ω)**	**C1 (F)**	**n1**	**C2 (F)**	**n2**	**χ^2**
Y_3NbO_7 dry air	232	47850	18942	$1.9 \cdot 10^{-11}$	0.92289	$4.1 \cdot 10^{-5}$	0.66180	$3 \cdot 10^{-4}$
Y_3NbO_7 wet air	986	43902	13094	$1.9 \cdot 10^{-11}$	0.94287	$3.0 \cdot 10^{-5}$	0.72223	$3 \cdot 10^{-4}$
$Y_3Nb_{0.85}Ti_{0.15}O_{7-\delta}$ dry air	1322	14178	2852	$2.3 \cdot 10^{-11}$	0.93390	$7.1 \cdot 10^{-5}$	0.90125	$3 \cdot 10^{-4}$
$Y_3Nb_{0.85}Ti_{0.15}O_{7-\delta}$ wet air	878	12473	2238	$2.2 \cdot 10^{-11}$	0.94834	$8.0 \cdot 10^{-5}$	0.92905	$7 \cdot 10^{-4}$

Measured conductivity σ_m was determined by using equation (2):

$$\sigma_m = \frac{1}{\rho} = \frac{l}{RS} \qquad (2)$$

where resistance R is the width of the higher frequency semicircle in a complex impedance plot, l is the sample thickness and S is the electrode area. Bruggeman asymmetric model was applied for porosity correction [21,22]. Equation (3) was used, where σ_m is measured conductivity and p is the porosity fraction of the sample.

$$\sigma = \sigma_m \times (1 - p)^{-3/2} \qquad (3)$$

The activation energy E_A of the conductivity was calculated on the basis of the Arrhenius equation (4):

$$\sigma = \frac{\sigma_0}{T} exp\left(-\frac{E_A}{kT}\right) \qquad (4)$$

The Arrhenius-type plots of the temperature dependencies of the total conductivity for Y_3NbO_7 and $Y_3Nb_{0.85}Ti_{0.15}O_{7-\delta}$ as well as for $Y_3Nb_{0.98}Ti_{0.02}O_{7-\delta}$, $Y_3Nb_{0.96}Ti_{0.04}O_{7-\delta}$, $Y_3Nb_{0.94}Ti_{0.06}O_{7-\delta}$ and $Y_3Nb_{0.92}Ti_{0.08}O_{7-\delta}$ measured in the wet and dry air are presented in Fig. 7, and Fig. 8, respectively. The activation energies and selected conductivity values for the studied materials are gathered in Table 3 for measurements taken in air, and in Table 4 for measurements taken in hydrogen. It can be seen that conductivity depends on the temperature and two ranges of linear dependency can be distinguished for both wet and dry conditions: lower temperature range 350°C to 500°C and higher temperature range 550°C to 750°C. In the higher temperature range, measurements taken in the wet and dry air gave similar values of the conductivity. However, in the case of both specimens conductivity in wet atmospheres was slightly higher and the activation energy was lower than in dry ones. This difference is even more pronounced in the lower temperature range.

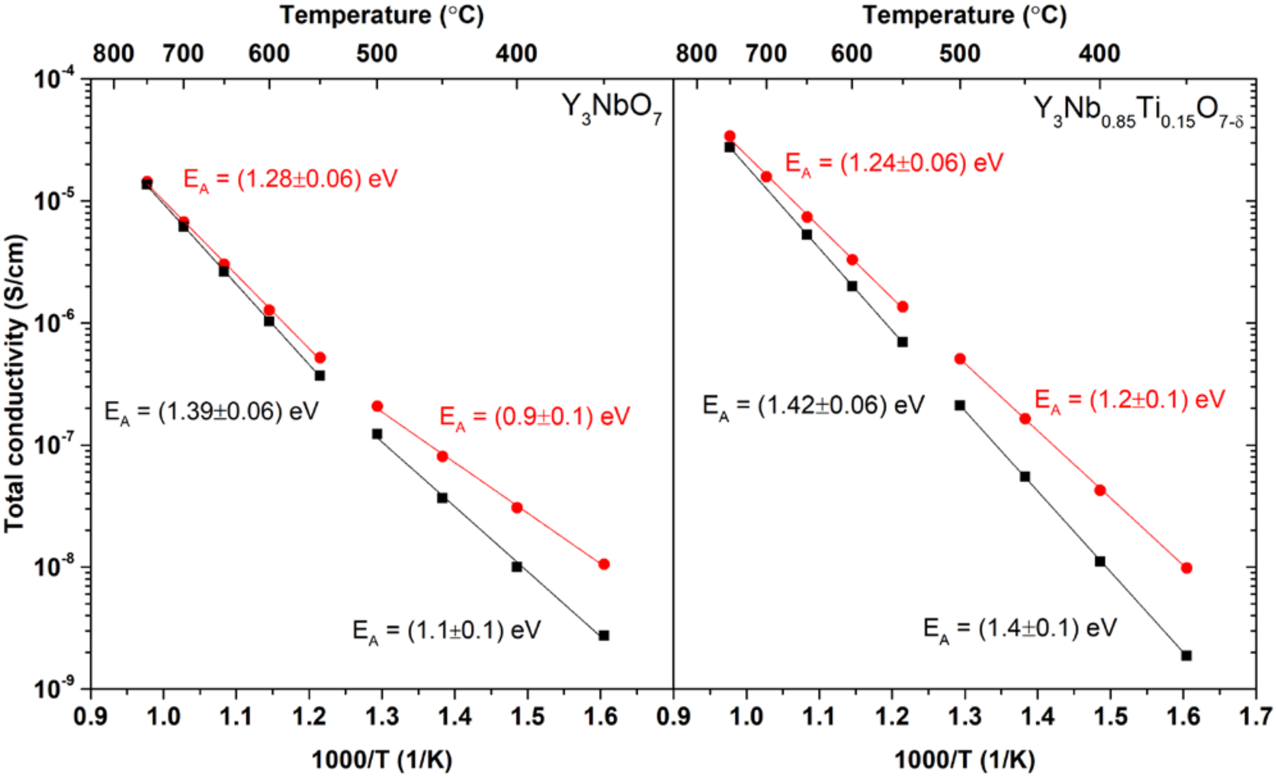

Fig. 7 Total conductivity of the samples with 0 and 15 mol% of Ti plotted as a function of inverse temperature. Circles and squares represent measurements in wet and dry air, respectively.

For all samples apart from the sample with the highest Ti content ($Y_3Nb_{0.85}Ti_{0.15}O_{7-\delta}$), the activation energies in wet air at high temperatures generally decrease with increasing titanium content, whereas in dry atmospheres they vary only within the uncertainty limit. In the low-temperature range, the influence of Ti content is less obvious and no clear trend could be derived from the data. However, in wet conditions, the activation energy generally decreases with increasing Ti content reaching the minimum for 5 mol% Ti. The activation energy in the dry atmosphere shows no trend whatsoever.

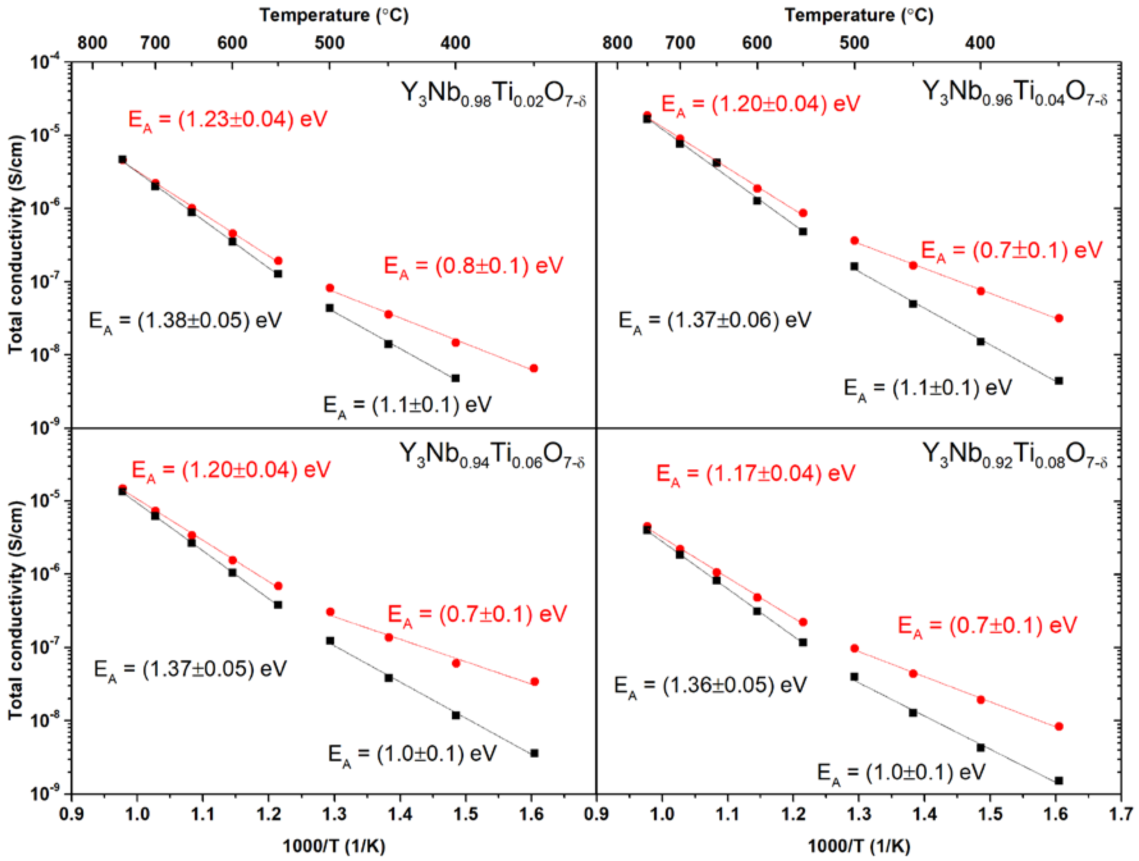

Fig.8 Total conductivity of the samples with 2, 4, 6 and 8 mol% of Ti plotted as a function of inverse temperature. Circles and squares represent measurements in wet and dry air, respectively.

Total conductivity of the samples with titanium content between 2 and 8 mol% was also measured in wet and dry hydrogen. Arrhenius-type plots are presented in Fig.9. Both the values of conductivity and the activation energies are higher in comparison with those obtained in air. Moreover, in the high-temperature range the total conductivity in dry hydrogen is higher than in wet hydrogen, whereas, in the lower temperature range, the relation between the conductivities is opposite.

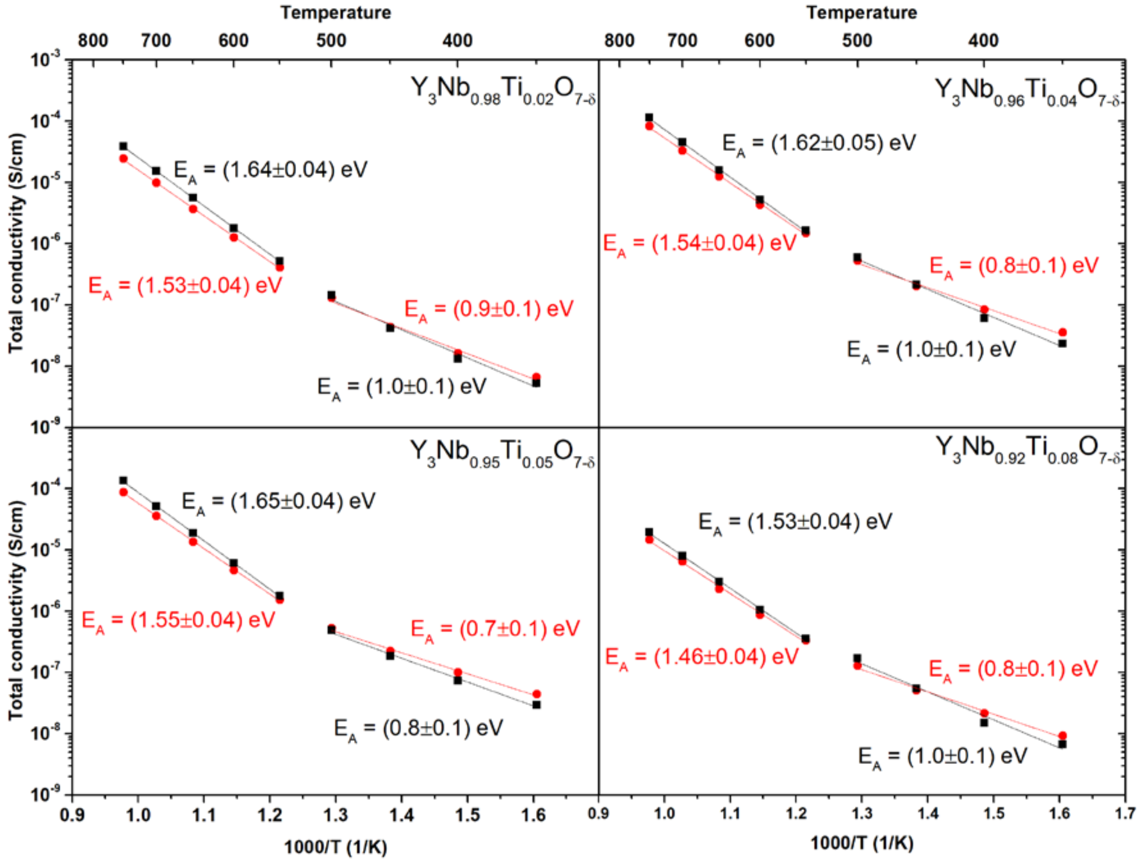

Fig.9 Total conductivity of the samples with 2, 4, 5 and 8 mol% of Ti plotted as a function of inverse temperature. Circles and squares represent measurements in wet and dry hydrogen, respectively.

Table 3 The activation energies and conductivities measured in air.

Sample	E_A (eV)		σ (Scm^{-1} x 10^{-5})	E_A (eV)		σ (Scm^{-1} x 10^{-7})
	750°C - 550°C		750 °C	500°C - 350°C		450 °C
	Wet air	Dry air	Wet air	Wet air	Dry air	Wet air
Y_3NbO_7	1.28(3)	1.39(5)	1.4(1)	0.9(1)	1.1(1)	0.8(1)
$Y_3Nb_{0.99}Ti_{0.01}O_{7-\delta}$	1.23(4)	1.36(6)	0.6(1)	0.8(1)	0.8(1)	0.4(1)
$Y_3Nb_{0.98}Ti_{0.02}O_{7-\delta}$	1.23(4)	1.38(5)	0.5(1)	0.8(1)	1.1(1)	0.4(1)
$Y_3Nb_{0.97}Ti_{0.03}O_{7-\delta}$	1.24(3)	1.37(6)	2.4(1)	0.8(1)	1.0(1)	1.8(1)
$Y_3Nb_{0.96}Ti_{0.04}O_{7-\delta}$	1.20(4)	1.37(6)	1.9(1)	0.7(1)	1.1(1)	1.7(1)
$Y_3Nb_{0.95}Ti_{0.05}O_{7-\delta}$	1.20(6)	1.23(6)	1.6(1)	0.6(1)	0.9(1)	2.5(1)
$Y_3Nb_{0.94}Ti_{0.06}O_{7-\delta}$	1.20(4)	1.37(5)	1.5(1)	0.7(1)	1.0(1)	1.4(1)
$Y_3Nb_{0.92}Ti_{0.08}O_{7-\delta}$	1.17(4)	1.36(5)	0.5(1)	0.7(1)	1.0(1)	0.4(1)
$Y_3Nb_{0.90}Ti_{0.10}O_{7-\delta}$	1.17(3)	1.38(5)	0.9(1)	0.7(1)	0.9(1)	1.1(1)
$Y_3Nb_{0.85}Ti_{0.15}O_{7-\delta}$	1.24(6)	1.38(6)	3.4(1)	1.2(1)	1.4(1)	1.7(1)

Table 4 The activation energies and conductivities measured in hydrogen.

Sample	E_A (eV)		σ (Scm^{-1} x 10^{-5})	E_A (eV)		σ (Scm^{-1} x 10^{-7})
	750°C - 550°C		750 °C	500°C - 350°C		450 °C
	Wet H_2	Dry H_2	Wet H_2	Wet H_2	Dry H_2	Wet H_2
$Y_3Nb_{0.98}Ti_{0.02}O_{7-\delta}$	1.53(4)	1.64(4)	2.4(1)	0.9(1)	1.0(1)	0.4(1)
$Y_3Nb_{0.96}Ti_{0.04}O_{7-\delta}$	1.54(4)	1.62(5)	8.3(1)	0.8(1)	1.0(1)	2.0(1)
$Y_3Nb_{0.95}Ti_{0.05}O_{7-\delta}$	1.55(4)	1.65(4)	8.8(1)	0.7(1)	0.8(1)	2.2(1)
$Y_3Nb_{0.92}Ti_{0.08}O_{7-\delta}$	1.46(4)	1.53(4)	1.5(1)	0.8(1)	1.0(1)	0.5(1)

Examples of the conductivity at 450°C and 750°C, as well as the lattice constant, plotted as a function of Ti content are presented in Fig.10. There are two characteristic minima of conductivity for the samples containing about 2-3 and 8% of titanium. These minima are observed in each sample in the whole studied temperature range and in both atmospheres.

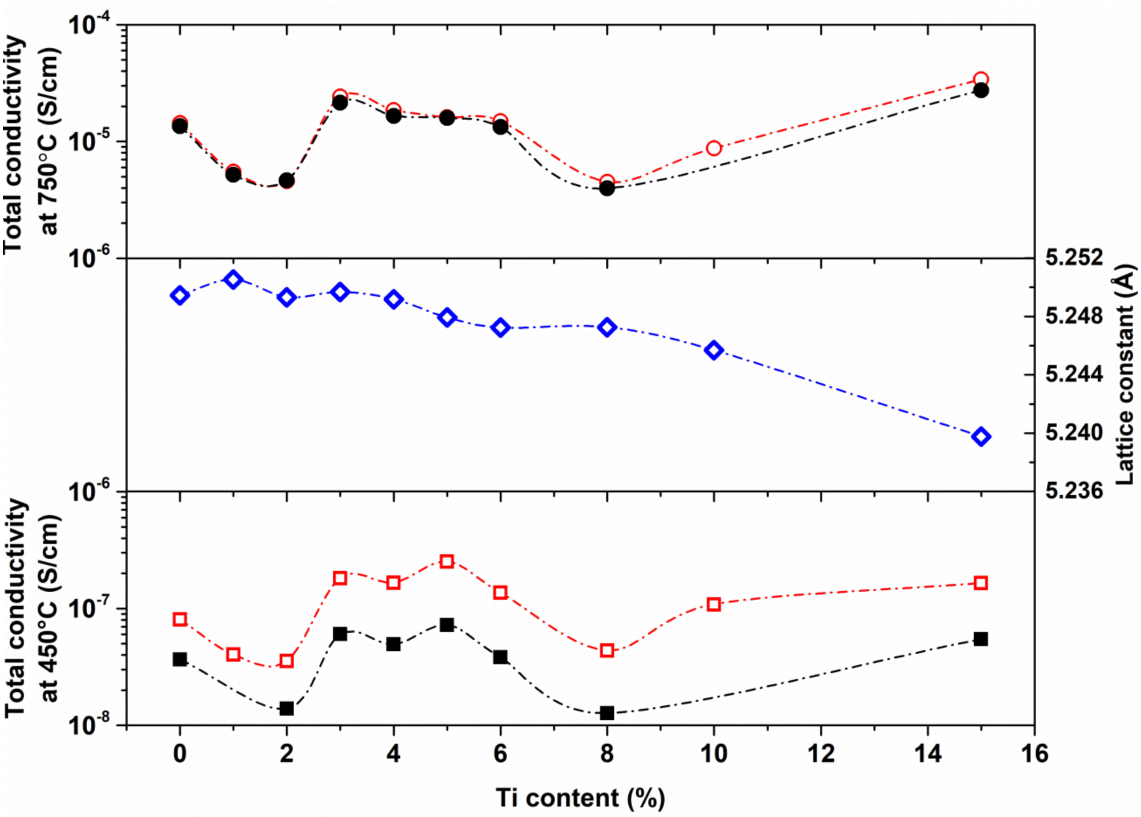

Fig. 10 Total conductivities and lattice constant dependence. Open symbols – wet air, closed symbols – dry air. Circles – temperature 750°C, squares – temperature 450°C.

4. Discussion

The results reported in this work show that electrical properties of the $Y_3Nb_{1-x}Ti_xO_{7-\delta}$ oxides depend on the atmosphere and temperature as well as on the titanium content.

The dependence of total electrical conductivity on the atmosphere may give a clue to understanding what types of charge carriers are responsible for the conductivity. First, we will discuss the influence of the presence of water in the atmosphere. Previous works carried out on undoped Y_3NbO_7 showed that it is an oxygen ion conductor with the activation energy of oxygen migration 1.33 eV [1,8], whereas in wet atmospheres proton conductivity was observed with proton migration activation energy 0.67 eV [8]. In the titanium-doped yttrium niobates studied in this work also the influence of wet atmospheres on the conductivity and its activation energy was observed which suggests that hydration of the oxygen vacancies takes place when the material is exposed to water vapour:

$$O_O^X + v_O^{\cdot\cdot} + H_2O_{(g)} = 2OH_O^{\cdot} \qquad (5)$$

Activation energies of conductivity observed at temperatures below 500° C in wet atmospheres were for most samples between 0.6 eV and 0.9 eV whereas they were higher (between 0.8 eV and 1.1 eV) in dry atmospheres. This suggests that below 500° C both protons and oxygen ions contribute to the total conductivity but in wet atmospheres proton contribution is dominant. This is also supported by a difference between the conductivity values obtained in wet and dry atmospheres. In the low-temperature range conductivity in the wet atmosphere is higher than in a dry one. In the higher temperature range activation energies are higher (1.2 eV - 1.65 eV) whereas the differences between their values in wet and dry atmospheres are much lower (e.g. 1.24 eV and 1.37 eV for $Y_3Nb_{0.97}Ti_{0.03}O_{7-\delta}$ in the wet and dry air, respectively). Therefore, the contribution of protons to the total conductivity is low but still observed. A decrease in proton conductivity at high temperatures is commonly seen in various proton conductors and is usually attributed to increasing of oxygen or/and electron contribution to the conductivity which acts parasitically to proton conduction [23,24]. Summing up, in the air the $Y_3Nb_{1-x}Ti_xO_{7-\delta}$ oxides exhibit mixed oxygen-ion and proton conductivity.

The undoped Y_3NbO_7 oxide is an electronic insulator and a purely ionic conductor. Because of the titanium presence and its susceptibility to a valence change in reducing atmospheres, electronic-type conductivity may be also present. Discussion of the influence of the simultaneous presence of hydrogen and water vapour on the conductivity requires analysis of the relations between partial pressures of O_2, H_2, and H_2O. By utilizing the mass-action law on the reaction of water formation from hydrogen and oxygen:

$$H_2 + \frac{1}{2}O_2 = H_2O \qquad (6)$$

the following proportionality can be derived: $p_{O_2} \sim \frac{p_{H_2O}}{p_{H_2}}$. On this basis, it can be seen that while switching from wet to dry hydrogen both oxygen and water vapour partial pressures decrease.
The electronic contribution of $Y_3Nb_{1-x}Ti_xO_{7-\delta}$ oxides to the total conductivity may be expected to increase with the increase of the concentration of titanium ions with different valency states (+3 and +4). Assuming that titanium in the as-received samples is predominantly +4, decreasing p_{O_2} should lead to an increase in electronic conductivity. Therefore, partial electronic conductivity should increase with decreasing p_{O_2}, whereas protonic should decrease with decreasing p_{H_2O}. Since in the high-temperature range the total conductivity increases while switching from wet to dry hydrogen it indicates that electrons contribute significantly to the total conductivity. In the low-temperature range, the trend is opposite, which suggests that protons still dominate the total conductivity in low oxygen partial pressures. Since the difference between the conductivities in a wet and dry hydrogen atmosphere is smaller than in the case of oxidizing conditions it can be qualitatively stated that the material shows properties of a mixed protonic-electronic conductor in reducing conditions.

Understanding how the titanium content influences electrical properties of $Y_3Nb_{1-x}Ti_xO_{7-\delta}$ requires complex analysis of several interrelated factors. The observed non-monotonic dependencies of the total conductivity values at different temperatures (Fig. 10) and activation energies (Tables 3,4) on the titanium content indicate that at least two factors influence the properties in opposite ways. Moreover, the unit cell parameters exhibit also non-monotonicity, which implies that the structural analysis is crucial for the interpretation of the observed properties. Total electrical conductivity is a sum of the contributions of all relevant types of charge carriers, where each partial conductivity depends on the concentration and mobility of charge carriers. Roughly speaking, the titanium and oxygen vacancy contents as well as the distribution of the titanium valence states in $Y_3Nb_{1-x}Ti_xO_{7-\delta}$ are expected to directly affect the charge carriers' concentration and indirectly, through the structural effects, - the mobility. Moreover, the presence of titanium influenced the grain size of the ceramics in such a way, that the grains in Y_3NbO_7 were twice as large as in the titanium-doped samples. However, the grain boundary contribution was not observed in the measurements, but such a large difference in microstructure affects so many properties that it seems correct to exclude the Y_3NbO_7 sample from the further discussion.

Titanium in $Y_3Nb_{1-x}Ti_xO_{7-\delta}$ is an acceptor-type dopant, and its charge is expected to be compensated mainly by oxygen vacancies:

$$\frac{3}{2}Y_2O_3 + xTiO_2 + \frac{1-x}{2}Nb_2O_5 = 3Y_Y^{\mathrm{x}} + xTi'_{Nb} + (1-x)Nb_{Nb}^{\mathrm{x}} + \frac{x}{2}v_O^{\cdot\cdot} + \left(7-\frac{x}{2}\right)O_O^{\mathrm{x}} \quad (7)$$

So that, the oxygen vacancies concentration increases with the increasing titanium content. In view of the results of Kobayashi et al. [11] who found that the conductivity of the Y_3NbO_7 ceramics increased almost linearly with an increase of the oxygen vacancies concentration, a monotonic dependence of conductivity in the dry air on the titanium content could be expected. Similarly, in wet atmospheres proton conductivity should increase with the titanium content thanks to increasing the number of vacancies available for hydration. In the case of the $Y_3Nb_{1-x}Ti_xO_{7-\delta}$ oxides conductivity of the samples containing a very low Ti content ($x<0.03$) is low, whereas it is the highest for x between 0.03 and 0.06 and for x=0.10 and 0.15. Another compositional region in which the conductivity is very low is about x = 0.08. This means that the competition between the factors increasing the conductivity (that is oxygen vacancy concentration) and decreasing the conductivity is not straightforward. Two groups of structural changes related to the presence of titanium should be considered: distortions from the defect-fluorite structure and defect clustering.

The structural analysis carried out by Lee et al. [1] have shown that Y_3NbO_7 contains small regions with some local ordering different from the defect-fluorite type. This was further investigated by Lopez-Conesa et al. in RE_3NbO_7 (RE = Y, Er, Yb, Lu) [7]. They found the existence of the microdomains of sizes below the XRD sensitivity with short-range pyrochlore ordering accompanying the long-range fluorite ordering. In order to discuss such a possibility in the case of $Y_3Nb_{1-x}Ti_xO_{7-\delta}$ oxides, one should take into consideration two end members for analysed structure: defect fluorite Y_3NbO_7 and pyrochlore $Y_2Ti_2O_7$. As is known from the previous research, for the smaller cations in rare earth niobates series the energetics of formation of RE_3NbO_7 and $RE_2Ti_2O_7$ is similar (the formation enthalpies are almost equal) [6]. Therefore, from the thermodynamic points of view, the formation of both these structures is equally favourable. Knowing that even Y_3NbO_7 exhibits short-range pyrochlore ordering, we suggest that the titanium presence promotes forming the pyrochlore domains within the structure.

The other phenomena, which one should consider, are the possible vacancy clustering or/and vacancy position within the compound structure. For Y_3NbO_7 the vacancies presumably would be neighboured by yttrium 3+ preferentially to niobium 5+ because the lower charge difference would be beneficial from the lattice energetics point of view. It may be also supported by the results of the Molecular Dynamics analysis carried out by Marocchelli et al. who showed that in Y_3NbO_7 the Y-O bonds are longer, i.e. weaker, than the Nb-O bonds [13]. They also showed that the oxygen ions located in tetrahedral sites with all the vertices occupied by Y3+ cations are immobile. Substitution of Nb5+ with titanium ions decreases the effective charge of the (Nb, Ti) sites, which may be expected to change the distribution of the oxygen vacancies. The complex structural properties may be also related to two or more oxygen vacancy sites present within the structure. Some of the vacancies can be presumably taking part in proton and oxygen ion conductions and some of them cannot. Therefore, the differentiation between such sites would be necessary to understand the influence of the structure on the electrical performance of the material.

5. Conclusions

Series of titanium-doped yttrium niobates ($Y_3Nb_{1-x}Ti_xO_{7-\delta}$) samples were synthesized through the solid-state reaction method. The titanium content varied from x = 0 to x = 0.15. The X-ray diffraction data have shown that all samples where $x \leq 0.15$ are single phase.

The $Y_3Nb_{1-x}Ti_xO_{7-\delta}$ oxides in the air atmosphere exhibit mixed oxygen-ion and proton conductivity, whereas in reducing conditions they show properties of mixed protonic-electronic conductors. The proton conductivity dominated in the low-temperature range in wet atmospheres.

Non-monotonic dependence of the total conductivity on titanium content was observed. It was found that the conductivity of the $Y_3Nb_{1-x}Ti_xO_{7-\delta}$ samples with x between 0.03 and 0.06 and for x=0.10 and 0.15 achieved the highest values both in the wet and dry air. This was interpreted as a result of the competition between the factors promoting- and hindering the conductivity. The increasing titanium content caused an increase in the oxygen vacancy concentration which promoted the conductivity. On the other hand, two groups of structural changes related to the presence of titanium, that is, distortions from the defect-fluorite structure and defect clustering were considered as possible reasons for impeding the conductivity.

Acknowledgments

This research was partially funded by National Science Centre, Poland - Grant No.

2016/23/B/ST5/02137

References

[1] J. Lee, M. Yashima, M. Yoshimura, Ionic conductivity of fluorite-structured solid solution $Y_{0.8}Nb_{0.2}O_{1.7}$, Solid State Ionics. 107 (1998) 47–51. doi:http://dx.doi.org/10.1016/S0167-2738(97)00529-8.

[2] T. Okubo, M. Kakihana, Low temperature synthesis of Y_3NbO_7 by polymerizable complex method: Utilization of a methanol-citric acid solution of $NbCl_5$ as a novel niobium precursor, J. Alloys Compd. 256 (1997) 151–154. doi:10.1016/S0925-8388(96)02986-6.

[3] H. Yamamura, Electrical conductivity of the systems, $(Y_{1-x}M_x)_3NbO_7$ (M=Ca, Mg) and $Y_3Nb_{1-x}M_xO_7$ (M′=Zr and Ce), Solid State Ionics. 123 (1999) 279–285. doi:10.1016/S0167-2738(99)00098-3.

[4] Raghvendra, P. Singh, Electrical conductivity of YSZ-SDC composite solid electrolyte synthesized via glycine-nitrate method, Ceram. Int. 43 (2017) 11692–11698. doi:10.1016/j.ceramint.2017.05.359.

[5] H. Deng, W. Zhang, X. Wang, Y. Mi, W. Dong, W. Tan, B. Zhu, An ionic conductor $Ce_{0.8}Sm_{0.2}O_{2-\delta}$(SDC) and semiconductor $Sm_{0.5}Sr_{0.5}CoO_3$(SSC) composite for high performance electrolyte-free fuel cell, Int. J. Hydrogen Energy. 42 (2017) 22228–22234. doi:10.1016/j.ijhydene.2017.03.089.

[6] A. Mielewczyk-Gryn, A. Navrotsky, Enthalpies of formation of rare earth niobates, RE_3NbO_7, Am. Mineral. 100 (2015) 1578–1583. doi:http://dx.doi.org/10.2138/am-2015-5210.

[7] L. López-Conesa, J.M. Rebled, M.H. Chambrier, K. Boulahya, J.M. González-Calbet, M.D. Braida, G. Dezanneau, S. Estradé, F. Peiró, Local Structure of Rare Earth Niobates (RE_3NbO_7, RE = Y, Er, Yb, Lu) for Proton Conduction Applications, Fuel Cells. 13 (2013) 29–33. doi:10.1002/fuce.201200136.

[8] A. Chesnaud, M.D. Braida, S. Estradé, F. Peiró, A. Tarancón, A. Morata, G. Dezanneau, High-temperature anion and proton conduction in RE_3NbO_7 (RE=La, Gd, Y, Yb, Lu) compounds, J. Eur. Ceram. Soc. 35 (2015) 3051–3061. doi:10.1016/j.jeurceramsoc.2015.04.014.

[9] M. Inabayashi, Y. Doi, M. Wakeshima, Y. Hinatsu, Synthesis, crystal structures and magnetic properties of fluorite-related compounds Ce_3MO_7(M = Nb, Ta), J. Solid State Chem. 254 (2017) 150–154. doi:10.1016/j.jssc.2017.07.022.

[10] A. Walasek, E. Zych, J. Zhang, S. Wang, Synthesis, morphology and spectroscopy of cubic Y_3NbO_7:Er, J. Lumin. 127 (2007) 523–530. doi:10.1016/j.jlumin.2007.02.063.

[11] H. Kobayashi, H. Ogino, T. Mori, H. Yamamura, T. Mitamura, Preparation of Y_3NbO_7 Powders

with Excess Conductivity of the Sintered Oxygen Bodies, J. Ceram. Soc. Japan. 101 (1993) 671–674.

[12] L. Cai, J.C. Nino, Structure and dielectric properties of Ln_3NbO_7 (Ln = Nd, Gd, Dy, Er, Yb and Y), J. Eur. Ceram. Soc. 27 (2007) 3971–3976. doi:10.1016/j.jeurceramsoc.2007.02.077.

[13] D. Marrocchelli, P. Madden, S.T. Norberg, S. Hull, Cation composition effects on oxide conductivity in the $Zr_2Y_2O_7$-Y_3NbO_7 system., J. Phys. Condens. Matter. 21 (2009) 405403. doi:10.1088/0953-8984/21/40/405403.

[14] S. Hull, S.T. Norberg, I. Ahmed, S.G. Eriksson, D. Marrocchelli, P.A. Madden, Oxygen vacancy ordering within anion-deficient Ceria, J. Solid State Chem. 182 (2009) 2815–2821. doi:10.1016/j.jssc.2009.07.044.

[15] H.P. Rooksby, E.A.D. White, Rare-Earth Niobates and Tantalates of Defect Fluorite- and Weberite-Type Structures, J. Am. Ceram. Soc. 47 (1964) 94–96. doi:10.1111/j.1151-2916.1964.tb15663.x.

[16] XPSPEAK 4.1, www.phy.cuhk.edu.hk/~surface/XPSPEAK.

[17] S. Wachowski, A. Mielewczyk-Gryn, M. Gazda, Effect of isovalent substitution on microstructure and phase transition of $LaNb_{1-x}M_xO_4$ (M=Sb, v or Ta; X=0.05-0.3), J. Solid State Chem. 219 (2014) 201–209. doi:10.1016/j.jssc.2014.07.041.

[18] B. Le Diard, J.-P.Gorrec, C. Montella, Handbook of Electrochemical Impedance Spectroscopy ELECTRICAL CIRCUITS, (2013) 33. http://www.bio-logic.info/potentiostat-electrochemistry-ec-lab/apps-literature/eis-literature/hanbook-of-eis/.

[19] C.D. Wagner, W.M. Riggs, L.E. Davis, J.F. Moulder, Handbook of X-Ray Photoelectron Spectroscopy, (1979) 1990. doi:10.1002/sia.740030412.

[20] J.T.S. Irvine, D.C. Sinclair, A.R. West, Electroceramics: Characterization by Impedance Spectroscopy, Adv. Mater. 2 (1990) 132–138. doi:10.1002/adma.19900020304.

[21] D.A.G. Bruggeman, Berechnung verschiedener physikalischer Konstanten von heterogenen Substanzen I. Dielektrizitatskonstanten und Leitfahigkeiten der Mischkorper aus isotropen Substanzen, Ann. Phys. 416 (1935) 636–664. doi:10.1002/andp.19354160705.

[22] A. Mielewczyk-Gryn, T. Lendze, K. Gdula-Kasica, P. Jasinski, A. Krupa, B. Kusz, M. Gazda, Characterization of $CaTi_{0.9}Fe_{0.1}O_3/La_{0.98}Mg_{0.02}NbO_4$ composite, Open Phys. 11 (2013) 213–218. doi:10.2478/s11534-012-0152-6.

[23] S. Wachowski, A. Mielewczyk-Gryń, K. Zagórski, C. Li, P. Jasiński, S.J. Skinner, R. Haugsrud, M. Gazda, Influence of Sb-substitution on ionic transport in lanthanum orthoniobates, J. Mater. Chem. A. 4 (2016) 11696–11707. doi:10.1039/C6TA03403A.

[24] K. Gdula-Kasica, A. Mielewczyk-Gryn, S. Molin, P. Jasinski, A. Krupa, B. Kusz, M. Gazda, Optimization of microstructure and properties of acceptor-doped barium cerate, in: Solid State

Ionics, 2012: pp. 245–249.